MOX–Report No. 54/2012

Spatial regression models over two-dimensional manifolds

Ettinger, B., Perotto, S.; Sangalli, L.M.

MOX, Dipartimento di Matematica "F. Brioschi"
Politecnico di Milano, Via Bonardi 9 - 20133 Milano (Italy)

mox@mate.polimi.it http://mox.polimi.it

Spatial regression models over two-dimensional manifolds*

Bree Ettinger[♯], Simona Perotto[♯], Laura M. Sangalli[♯]

November 29, 2012

[♯] MOX– Modellistica e Calcolo Scientifico
Dipartimento di Matematica "F. Brioschi"
Politecnico di Milano
via Bonardi 9, 20133 Milano, Italy
bree.ettinger@polimi.it
simona.perotto@polimi.it
laura.sangalli@polimi.it

Keywords: Analysis of Object Data, Functional Data Analysis, spatial data analysis, penalized regression, partial differential regularization, finite elements.

Abstract

We propose a regression model for data spatially distributed over non-planar two-dimensional Riemannian manifolds. The model is a generalized additive model with a roughness penalty term involving a suitable differential operator computed over the non-planar domain. Thanks to a semi-parametric framework, the model allows for inclusion of space-varying covariate information. We show that the estimation problem can be solved first by conformally mapping the non-planar domain to a planar domain and then by applying existing models for penalized spatial regression over planar domains, appropriately modified to account for the domain deformation. The flattening map and the estimation problem are both computed by resorting to a finite element approach. The estimators are linear in the observed data values and classical inferential tools are derived. The application driving this research is the study of hemodynamic forces on the wall of an internal carotid artery affected by an aneurysm.

*This work has been funded by MIUR Ministero dell'Istruzione dell'Università e della Ricerca, *FIRB Futuro in Ricerca* research project "Advanced statistical and numerical methods for the analysis of high dimensional functional data in life sciences and engineering" (see http://mox.polimi.it/∼sangalli/firb.html), and by the program Dote Ricercatore Politecnico di Milano - Regione Lombardia, research project "Functional data analysis for life sciences".

1 Introduction and motivation

In this work, we present a new and innovative approach for modeling data that occur over non-planar two-dimensional domains. The applied problem driving this research is the study of hemodynamic forces, such as shear stress and pressure, exerted by blood-flow on the wall of an internal carotid artery. The data used in this study are part of the AneuRisk Project, a scientific endeavor that aimed at investigating the role of vessel morphology, blood fluid dynamics and biomechanical properties of the vascular wall, on the pathogenesis of cerebral aneurysms. See, e.g., [17] and [24] for a detailed description of the project. Cerebral aneurysms are deformations of cerebral vessels characterized by a bulge of the vessel wall. Figure 1 shows an internal carotid artery affected by an aneurysm. The shear stress exerted by the blood flow on the wall of the artery, at the systolic peak, is represented by a colormap. Each value refers to a point (x_1, x_2, x_3) on the bi-dimensional and non-planar artery wall. In [4], a first analysis of these data was performed, first by flattening the artery wall via a (bijective) angular map and then by applying standard spatial methods in the resulting planar domain. The angular map is equivalent to considering a simplified three-dimensional artery geometry, where the radius is fixed to a constant value and the curvature of the artery is not taken into account. This simplification can be a limiting factor since both the radius and curvature are geometrical quantities that greatly influence the hemodynamics in an artery as well as statistically discriminate aneurysm presence and location (see [24]). This suggests the need to develop an alternative approach that is able to take into account the actual geometry of the domain. Moreover, to obtain a bijective angular map, it is necessary to exclude the aneurysmal sac. This is a second critical issue which cannot be ignored in view of developing of more realistic studies.

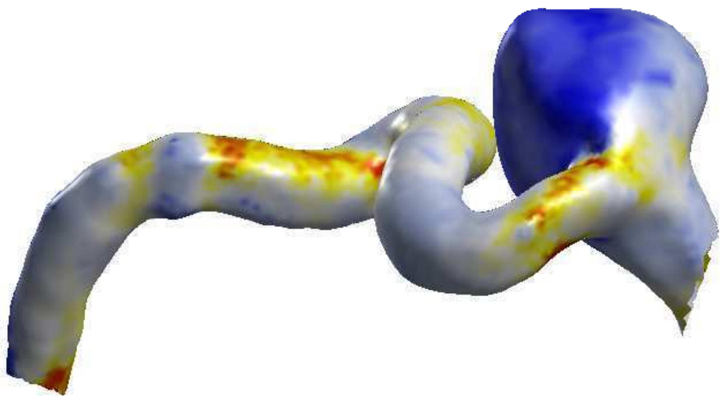

Figure 1: Shear stress exerted by blood flow on the wall of a carotid artery affected by aneurysms. The colormap shows the modulus of the wall shear stress at the systolic peak. The colormap ranges from 0 (blue) to 200 (red).

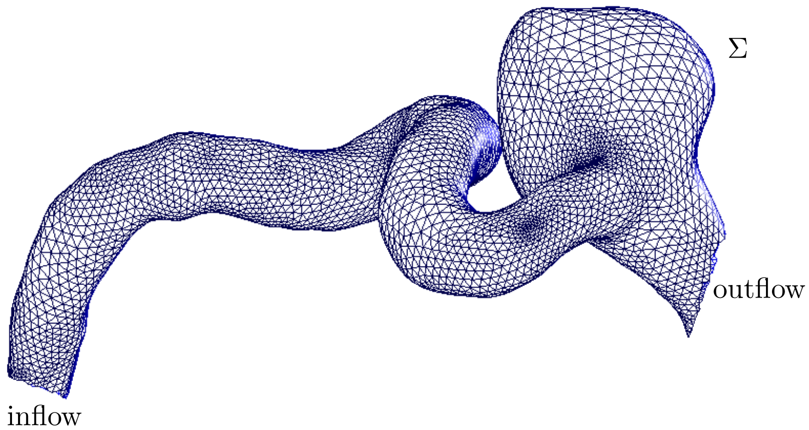

Figure 2: Reconstruction of the real internal carotid artery geometry in Figure 1 from a three-dimensional angiography via a VMTK reconstruction algorithm. The wall of the artery is approximated via a triangular mesh.

Few methods are available in literature to deal with data on non-planar domains. Non-planar domains can be approximated by three-dimensional triangular meshes characterized by varying distances and angles between neighboring vertices. Figure 2 displays an example of a triangular mesh that approximates the artery wall in Figure 1. Iterative schemes for nearest neighbor averaging have been developed to work on such surface meshes [11]. According to this approach, the value of the variable of interest at each vertex in the mesh is obtained by suitably averaging the values at the neighboring vertices. This process is repeated several times to create a smoothing effect. A more sophisticated method, heat kernel smoothing, is presented, e.g., in [6]. Heat kernel smoothing uses the eigenfunctions of the Laplace-Beltrami operator defined on the non-planar domain to construct a heat kernel. For each iteration, the amount of smoothing is determined by the bandwidth of the heat kernel. For large bandwidths, heat kernel estimates are comparable to the simpler and less computationally demanding method of nearest neighbor averaging [11]. On the other hand, the sophisticated structure of heat kernel smoothing has the advantage of providing powerful tools for statistical analysis. Other models have been devised to handle data over specific type of manifolds such as spheres. For instance, spherical splines introduced by [3], and the model described by [14].

Here, we adopt a Functional Data Analysis approach (see, e.g., [21] and [9]), and propose a regression method that efficiently handles data distributed over Riemannian manifolds. In particular, we generalize the spatial regression models developed in [22] and [23] to the case of non-planar domains, by defining a penalized spatial regression model where the roughness penalty term involves a suitable differential operator computed over the non-planar domain. The key idea consists of solving the estimation problem by conformally mapping the non-planar domain to a planar domain and then by applying the spatial regression model over planar domains properly modified to account for the actual geometry. From a computational viewpoint, to calculate the flattening map and solve the equivalent estimation problem on the planar domain, we use a basis for continuous piecewise-polynomials provided by finite elements. The use of finite elements also leads to high computational efficiency. The penalized regression estimator is linear in the observed data values and the usual inferential tools are thus derived. Another important feature of the proposed model is the possibility to include space-varying covariate information in a straightforward way. A series of simulation studies, on both test domains and domains from real-geometries, show the good performance of the proposed methodology. These simulations also highlight the advantages in terms of improved estimates where the geometry of the non-planar domain is taken into account. Given the complexity of the objects considered (data and covariates spatially distributed over bi-dimensional Riemannian manifolds), our work can also be seen as an Analysis of Object Data, as defined in [26].

The paper is organized as follows. Section 2 introduces the model. Section 3 describes the flattening map and derives the equivalent estimation problem on a planar domain. Section 4 shows how to compute the flattening map and the estimator using finite elements. A covariate version of the model is developed in Section 5. Section 6 is devoted to simulation studies and to the application to the hemodynamic data. Section 7 states future research directions.

2 The model

Consider n fixed data locations $\{\mathbf{x}_i = (x_{1i}, x_{2i}, x_{3i}) : i = 1, \ldots, n\}$ lying on a non-planar domain Σ that is a uniformly regular surface embedded in $\mathbb{R}^3$. For each location $\mathbf{x}_i$, a real-valued random variable of interest, z_i, is observed. We assume the model

$$z_i = f(\mathbf{x}_i) + \epsilon_i, \qquad\qquad i = 1, \ldots, n, \tag{1}$$

where $\epsilon_i,\ i = 1, \ldots, n$, are independent observational errors with zero mean and constant variance σ^2, and f is a twice continuously differentiable real-valued function defined on the surface domain Σ. Our goal is to estimate the function f in (1). By analogy to the models in [22] and [23], referred to in the following as spatial regression models over planar domains, we propose to estimate f by minimizing the following penalized sum of squared error functional

$$J_{\Sigma,\lambda}(f) = \sum_{i=1}^{n} (z_i - f(\mathbf{x}_i))^2 + \lambda \int_{\Sigma} (\Delta_\Sigma f(\mathbf{x}))^2 \ d\Sigma, \tag{2}$$

where Δ_Σ is the Laplace-Beltrami operator for functions defined over the surface Σ (see, e.g., [8]). The Laplace-Beltrami operator is a generalization of the standard Laplacian (considered in the model over planar domains) to the case of functions defined on surfaces in Euclidean spaces and is related to the local curvature of f on Σ. Hence in (2), via the penalty, we are controlling the roughness of f. Moreover, the Laplace-Beltrami operator is invariant with respect to Euclidean transformations of the domain ensuring that the smoothness of the estimate does not depend on an arbitrary chosen coordinate system. We also note that the Laplace-Beltrami operator is the same operator used by heat kernel smoothing, although in a different framework.

In this paper, we show that it is possible to solve the estimation problem (2) by exploiting existing techniques over planar domains. The problem is equivalently reformulated on a planar domain by considering an appropriate change of variable from the surface domain Σ to a planar domain. To do this, the surface Σ is flattened by means of a conformal map and the roughness penalty in (2) is modified accordingly, to account for the domain deformation induced by the flattening.

3 The flattening map and the equivalent estimation problem on the planar domain

Consider a non-planar domain Σ that is a surface embedded in $\mathbb{R}^3$ defined by a uniformly regular and continuously differentiable map

$$\begin{aligned} X : \Omega &\to \Sigma \\ \mathbf{u} = (u, v) &\mapsto \mathbf{x} = (x_1, x_2, x_3), \end{aligned}$$

where Ω is an open, convex and bounded set in $\mathbb{R}^2$ and the boundary of Ω, denoted $\partial\Omega$, is piecewise C^∞. A generic point in the planar domain Ω is denoted by $\mathbf{u} = (u, v)$. Let $X_u(\mathbf{u})$ and $X_v(\mathbf{u})$ denote the column vectors in $\mathbb{R}^3$ of the first order partial derivatives of X with respect to u and v, respectively. For the regularity and differentiability hypotheses on X, there exists a positive constant η such that, for any point $\mathbf{u} \in \Omega$,

$$\mathcal{W}(\mathbf{u}) = |X_u(\mathbf{u}) \wedge X_v(\mathbf{u})| = \sqrt{\|X_u(\mathbf{u})\|^2 \|X_v(\mathbf{u})\|^2 - \langle X_v(\mathbf{u}), X_u(\mathbf{u})\rangle^2} \geq \eta, \quad (3)$$

where $|X_u(\mathbf{u}) \wedge X_v(\mathbf{u})|$ denotes the modulus of the cross product between $X_u(\mathbf{u})$ and $X_v(\mathbf{u})$, $\langle \cdot, \cdot \rangle$ is the Euclidean scalar product of two vectors and the corresponding norm is represented by $\| \cdot \|$. Figure 3 sketches the set up for the map X.

The Jacobian matrix of X is given by $\nabla X(\mathbf{u}) = (X_u(\mathbf{u}),\ X_v(\mathbf{u}))$ for any $\mathbf{u} \in \Omega$ and has maximal rank equal to two. Using the Jacobian, we define the (space varying) metric tensor $G(\mathbf{u})$ as the following symmetric positive definite matrix

$$G(\mathbf{u}) \quad = \quad \nabla X(\mathbf{u})' \nabla X(\mathbf{u}) = \begin{pmatrix} \|X_u(\mathbf{u})\|^2 & \langle X_u(\mathbf{u}), X_v(\mathbf{u})\rangle \\ \langle X_u(\mathbf{u}), X_v(\mathbf{u})\rangle & \|X_v(\mathbf{u})\|^2 \end{pmatrix}$$

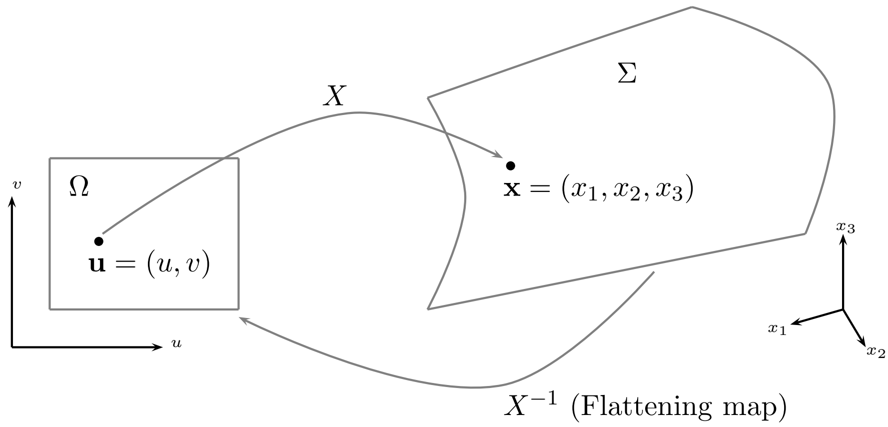

Figure 3: A sketch of the map X between Ω and Σ. The inverse X^{-1} of X, represents the flattening map.

for any $\mathbf{u} \in \Omega$, where $'$ denotes the transpose of a matrix. The inverse metric tensor $G^{-1}(\mathbf{u})$, which is also a symmetric positive definite matrix, is easily calculated as

$$G^{-1}(\mathbf{u}) = \frac{1}{[\mathcal{W}(\mathbf{u})]^2} \begin{pmatrix} \|X_v(\mathbf{u})\|^2 & -\langle X_u(\mathbf{u}), X_v(\mathbf{u})\rangle \\ -\langle X_u(\mathbf{u}), X_v(\mathbf{u})\rangle & \|X_u(\mathbf{u})\|^2 \end{pmatrix},$$

where $\mathcal{W}(\mathbf{u})$ is as in (3). Hence, $\mathcal{W}(\mathbf{u})$ has two meanings: $\mathcal{W}(\mathbf{u}) = \sqrt{\det(G(\mathbf{u}))}$ or $\mathcal{W}(\mathbf{u})$ coincides with as the modulus of cross product $X_u \wedge X_v$. With the former interpretation, we obtain the area element involved in the change of variable from Σ to Ω, i.e., $d\Sigma = \mathcal{W}(\mathbf{u})d\Omega$.

Let $f \circ X \in \mathcal{C}^2(\Omega)$; then the Σ-gradient of f is $\nabla_\Sigma f(\mathbf{x}) = \nabla X(\mathbf{u})\, G^{-1}(\mathbf{u}) \nabla f(X(\mathbf{u})) \in \mathbb{R}^3$ for any $x \in \Sigma$, where $\nabla f(X(\mathbf{u}))$ denotes the gradient of f on Ω and $\mathbf{u} = X^{-1}(\mathbf{x})$. For a tangential vector field Y, the Σ-divergence is given by

$$\mathrm{div}_\Sigma Y(\mathbf{x}) = \frac{1}{\mathcal{W}(\mathbf{u})} \sum_{j=1}^{2} \partial_j \mathcal{W}(\mathbf{u}) Y^j(X(\mathbf{u})),$$

where Y^j denotes the j-th direction of the tangential vector field, $\partial_1 = \frac{\partial}{\partial u}$ and $\partial_2 = \frac{\partial}{\partial v}$ (see, e.g., [8]). Then the Laplace-Beltrami operator can be expressed as

$$\begin{aligned} \Delta_\Sigma f(\mathbf{x}) &= \mathrm{div}_\Sigma(\nabla_\Sigma f(X(\mathbf{u}))) \\ &= \frac{1}{\mathcal{W}(\mathbf{u})} \sum_{j,m=1}^{2} \partial_j (k_{jm}(\mathbf{u}) \partial_m f(X(\mathbf{u}))) = \frac{1}{\mathcal{W}(\mathbf{u})} \mathrm{div}(\mathbf{K} \nabla f(X(\mathbf{u}))) \end{aligned} \tag{4}$$

where the operator div denotes the divergence for planar domains and $k_{jm}(\mathbf{u})$ are the components of the matrix $\mathbf{K}(\mathbf{u}) = \{k_{jm}(\mathbf{u})\}_{j,m=1,2} = \mathcal{W}(\mathbf{u})\, G^{-1}(\mathbf{u})$. Note that $\mathbf{K}(\mathbf{u})$ is a symmetric positive definite matrix for any $\mathbf{u} \in \Omega$ since $\mathcal{W}(\mathbf{u})$ is positive and $G^{-1}(\mathbf{u})$ inherits positive definiteness from $G(\mathbf{u})$.

Thus, by considering the map X, the estimation problem over the manifold Σ, associated with the minimization of the penalized sum of squared error functional (2), can be reformulated as follows:

Equivalent estimation problem over the planar domain. Find the function $f \circ X$, defined on Ω, that minimizes

$$J_{\Omega,\lambda}(f \circ X) = \sum_{i=1}^{n} \big(z_i - f(X(\mathbf{u}_i))\big)^2 + \lambda \int_\Omega \frac{1}{\mathcal{W}(\mathbf{u})} \Big(\mathrm{div}(\mathbf{K} \nabla f(X(\mathbf{u})))\Big)^2 d\Omega. \tag{5}$$

One special case of interest is obtained for conformal flattening maps. The map X is said to be conformal if u and v are orthogonal and scale equally in each direction; in particular, $\|X_u(\mathbf{u})\|^2 = \|X_v(\mathbf{u})\|^2$ and $\langle X_u(\mathbf{u}), X_v(\mathbf{u})\rangle = 0$, for any $\mathbf{u} \in \Omega$. A conformal map thus preserves angles, which in turn preserves shapes and important geometrical features of the domain. This special case reduces (3) to $\mathcal{W}(\mathbf{u}) = \|X_u(\mathbf{u})\|^2$ as well as $G(\mathbf{u}) = \mathcal{W}(\mathbf{u})\mathbf{I}_2$, $G^{-1}(\mathbf{u}) = [\mathcal{W}(\mathbf{u})]^{-1}\mathbf{I}_2$ and $\mathbf{K} = \mathbf{I}_2$, where $\mathbf{I}_m$ is the identity matrix of order m. The Laplace-Beltrami operator (4) also simplifies to $\Delta_\Sigma f(X(\mathbf{u})) = [\mathcal{W}(\mathbf{u})]^{-1} \Delta f(X(\mathbf{u}))$, where Δ is the standard Laplace operator associated with the two-dimensional domain Ω, i.e., $\Delta h = \partial^2 h/\partial u^2 + \partial^2 h/\partial v^2$ where $h \in \mathcal{C}^2(\bar{\Omega})$. Finally, for conformal coordinates, the estimation problem (5) over the planar domain reduces to finding the function $f \circ X$, defined on Ω, that minimizes

$$J_{\Omega,\lambda}(f \circ X) = \sum_{i=1}^{n} \big(z_i - f(X(\mathbf{u}_i))\big)^2 + \lambda \int_\Omega \left(\frac{1}{\sqrt{\mathcal{W}(\mathbf{u})}} \Delta f(X(\mathbf{u}))\right)^2 d\Omega. \tag{6}$$

It is evident that the estimation problem (6) is a generalization of the spatial regression models over planar domains. In particular, the roughness penalty term has been modified by $\mathcal{W}(\mathbf{u})$, to include the original geometry of Σ. Although less evident, (5) can also be seen as an extension of the penalized sum of squared error functional used in the planar version of the model.

3.1 Flattening tubular domains

Since our driving application features tubular-like domains, we here review a method for flattening tubular surfaces, developed in [12] to flatten a portion of the colon. The tubular surface, Σ, must have the same topology as an open ended cylinder and be embedded in $\mathbb{R}^3$ with genus zero (i.e., there are no self intersections or holes). The open ends of the cylinder, denoted by b_0 and b_1, represent the boundary of Σ and are homeomorphic to a circle. With these assumptions, Σ is conformally equivalent to a rectangle in $\mathbb{R}^2$.

Here, we briefly illustrate the construction of the conformal map X, provided in [12]. The map X is constructed in two phases. The first phase maps the surface Σ to an annulus that has b_0 and b_1 as its inner and outer boundaries, respectively (Figure 4, left and right, illustrates this first step). During this phase, the first conformal parameter, u, is characterized as the solution to a Laplace-like problem with mixed boundary conditions, i.e.,

$$\begin{cases} -\Delta_\Sigma u = 0 \text{ on } \Sigma \\ u = 0 \text{ on } b_0 \\ u = 1 \text{ on } b_1. \end{cases} \tag{7}$$

The second phase converts the annulus into a rectangle (Figure 5, left); in particular, v is characterized as the harmonic conjugate of u. This is done by cutting the surface Σ, or the corresponding annulus, along a curve C that runs from b_0 to b_1 such that u is strictly increasing along C. We know there exists such a cut by the maximum principle. The boundaries b_0 and b_1 together with the cut C form an oriented boundary, denoted by B. The oriented boundary B is created by circling around b_0, then along C, around b_1, and finally back down C in the opposite direction. The boundary B is a closed curve whose direction is determined by the orientation of the surface (see Figure 4, center). Hence, v is characterized as the solution to

$$\begin{cases} -\Delta_\Sigma v = 0 \text{ on } \Sigma \\ v(\zeta) = \int_{\zeta_0}^{\zeta} \frac{\partial u}{\partial \nu}\, ds \;\; \text{ on } B, \end{cases} \tag{8}$$

where $\zeta_0 \in b_0$ is a designated starting point of the boundary B, $\zeta \in B$, $\frac{\partial u}{\partial \nu}$ is the normal derivative of u and ds denotes the arc-length element along B.

3.2 Characterization of the estimation problem on planar domain

To guarantee the existence and the uniqueness of a solution to the estimation problem in (5), we have to introduce a suitable functional setting. In particular, we resort to a modification of the standard Sobolev space $H^m(\Omega)$, i.e., the space of functions defined on Ω which are in $L^2(\Omega)$ together with all their partial derivatives up to order m ([15]). The functional space we consider is $H^m_{n0,\mathbf{K}}(\Omega) = \{h \in H^m(\Omega) \,:\, \mathbf{K}\nabla h \cdot n = 0 \text{ on } \partial\Omega\} \subset H^m(\Omega)$, consisting of the $H^m(\Omega)$-functions with co-normal derivatives identically equal to zero on the whole $\partial\Omega$. The condition on the co-normal derivative on $\partial\Omega$ is equivalent to the condition that the normal derivative on the boundary of Σ vanishes, i.e., $\nabla_\Sigma h \cdot n = 0$ on $\partial\Sigma$.

Let $\mathbf{z} = (z_1, \ldots, z_n)'$ be the vector collecting the observed values in (1) for the quantity of interest. For any function h defined on Σ, such that $h \circ X$ is defined on Ω, we denote the column vector of evaluations of the function h at the n data locations $\mathbf{x}_i$ by

$$\mathbf{h}_n = \Big(h(\mathbf{x}_1), \ldots, h(\mathbf{x}_n)\Big)' = \Big(h(X(\mathbf{u}_1)), \ldots, h(X(\mathbf{u}_n))\Big)', \tag{9}$$

with $X(\mathbf{u}_i) = \mathbf{x}_i$. To ease the notation, in the following we understand the dependence on $\mathbf{u}$.

Proposition 3.1 *The estimator $\hat{f} \circ X$ that minimizes (5) over $H^2_{n0,\mathbf{K}}(\Omega)$ satisfies the relation*

$$\boldsymbol{\mu}_n' \hat{\mathbf{f}}_n + \lambda \int_\Omega \frac{1}{\mathcal{W}} \Big(\mathrm{div}\,(\mathbf{K}\nabla(\mu \circ X))\Big) \Big(\mathrm{div}\Big(\mathbf{K}\nabla(\hat{f} \circ X)\Big)\Big) d\Omega = \boldsymbol{\mu}_n' \mathbf{z} \tag{10}$$

for any μ defined on Σ such that $\mu \circ X \in H^2_{n0,\mathbf{K}}(\Omega)$ with $\boldsymbol{\mu}_n$ and $\hat{\mathbf{f}}_n$ defined according to (9). Moreover, the estimator $\hat{f} \circ X$ is unique.

Proof. See Appendix A. □

4 Computation of the flattening map and estimator

The flattening map described by (7)-(8) as well as the estimation problem (10) are infinite dimensional problems that cannot be solved analytically. Thus we follow a typical approach in functional data analysis and use a suitable basis expansion to reduce these infinite dimensional problems to finite dimensional ones. In particular, since (7)-(8) and (10) involve partial differential operators, we resort to a finite element basis. The finite element method is widely used in engineering applications (for an introduction to the finite element framework see, e.g., [7]). This approach is similar to that of univariate splines. The domain of interest (either planar or non-planar) is subdivided into a mesh of disjoint elements and the solution at hand is approximated via a globally continuous function which coincides with a polynomial of a certain degree on each element of the mesh, i.e., with a so-called piecewise polynomial. The discretized problem becomes computationally tractable thanks to a suitable choice of basis functions for the space of piecewise polynomials. Thanks to the intrinsic construction of the finite element space, finding the flattening map and solving the estimation problem (10) reduce to solving linear systems, and thus the penalized regression estimator is linear in the observed data values.

4.1 Finite Elements

Convenient domain partitions, in both the planar and non-planar settings, are provided by triangular meshes (see Figure 2 for an example of a non-planar triangular mesh). In the triangulation, two adjacent triangles either share a vertex or a complete edge and the union of all the triangles approximates the domain. The boundary of the domain and any interior holes are represented by a polygon generated by the outer edges of the triangulation.

Starting from a triangulation $\mathcal{T}$ of the domain, a locally supported finite element basis can be generated such that it spans the space of piecewise polynomials over $\mathcal{T}$. This finite element space denoted by $H^1_{\mathcal{T}}$, discretizes the infinite dimensional space H^1. In this paper, we use linear finite elements where each basis function ψ_j is associated with a triangle vertex (also referred to as a *node*) ξ_j, $j = 1, \ldots, N$. The basis function ψ_j coincides with a so-called hat function, namely a piecewise linear polynomial which takes the value one at the vertex ξ_j and the value zero on all the other vertices, i.e., $\psi_j(\xi_l) = \delta_{jl}$ where δ_{jl} is the Kronecker delta symbol.

Let $\boldsymbol{\psi} = (\psi_1, \ldots, \psi_N)'$ be the column vector of the N basis functions. Then, for each function $h \in H^1_{\mathcal{T}}$,

$$h(\cdot) = \sum_{j=1}^{N} h(\xi_j)\psi_j(\cdot) = \mathbf{h}'\boldsymbol{\psi}(\cdot), \tag{11}$$

where

$$\mathbf{h} = (h(\xi_1), \ldots, h(\xi_N))' \tag{12}$$

is the column vector of evaluations of h at the N nodes of the mesh. Each function in $H^1_{\mathcal{T}}$ is thus identified by its evaluations on the mesh nodes. This is a well-known property characterizing a so-called Lagrangian basis. Notice that the finite element space $H^1_{\mathcal{T}}$ is characterized by less regularity than the spaces involved in (7)-(8) and (10), i.e., subsets of H^2. This leads us to provide an equivalent formulation for (7)-(8) and (10) in H^1 (see Appendix E and (14), respectively).

4.2 Example of flattening

To obtain an equivalent formulation of problems (7)-(8), characterizing the conformal flattening map, suited for the employment of a finite element space, we use the classical result that u in (7) is the minimizer of the energy functional

$$E_D(u) = \frac{1}{2}\int_{\Sigma} \|\nabla_{\Sigma} u\|^2 d\Sigma \tag{13}$$

and the same result applies for v in (8) (see [12] and [8] for more details). Both the problems are discretized via a finite element space and the functions u and v are approximated via finite element functions. In particular, we start with a non-planar triangular mesh $\Sigma_{\mathcal{T}}$, that closely approximates the surface domain Σ. Additionally, the flattening method maps $\Sigma_{\mathcal{T}}$ to a planar triangulation of Ω denoted by $\Omega_{\mathcal{T}}$, without flipping or breaking any of the triangles. This conveniently sets up the estimation problem in the planar domain to be solved via finite elements.

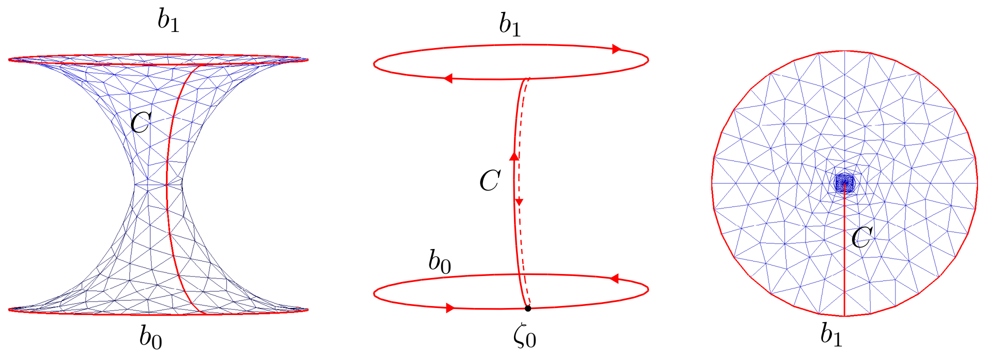

Figure 4: Left: three-dimensional triangular mesh approximating a non-planar test domain. Center: the oriented boundary B. Right: the annulus generated in the first phase of the flattening procedure.

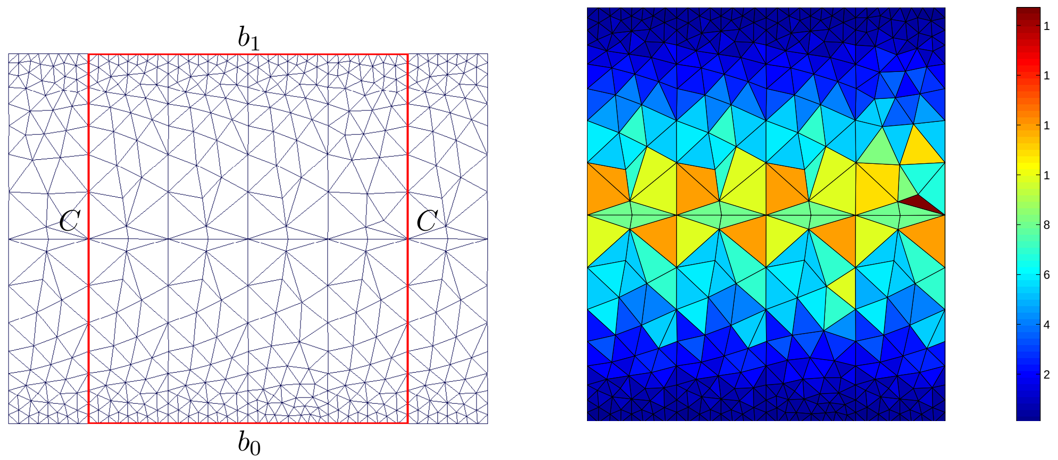

Figure 5: Left: the planar triangulated domain obtained by conformally flattening of the test domain in Figure 4. Right: the weights $\mathcal{W}(\mathbf{u})$ associated with the flattening conformal map.

The flattening procedure is detailed in Appendix E. Here, we only provide an example of the method. Figure 4 (left) shows a three-dimensional tubular test surface approximated by a triangular mesh. This test surface is generated with `gmsh` (see [10]) via a 180° rotation of the space between two non-intersecting circles. The boundary B, described in Section 3.1, is shown in red while its orientation is shown in Figure 4 (center). The annulus generated by finding the first conformal parameter u is shown in Figure 4 (right). This annulus has b_0 as its inner boundary (not clearly visible in the figure) and b_1 as its outer boundary. The rectangle generated by approximating the second conformal parameter v is shown in Figure 5 (left). Notice that the conformal rectangular domain has two artificial boundaries, generated by the cut C (the two vertical red sides). To easily obtain the necessary periodicity of the estimate along this artificial cut, the planar triangulation and the corresponding data values are repeated on each side of C. Notice that, thanks to the locally supported nature of a finite element basis, it is sufficient to repeat only a small portion of the triangulated domain. Figure 5 (right) shows the weights $\mathcal{W}(\mathbf{u})$ associated with the conformal flattening map.

4.3 Solution to the estimation problem

By introducing a proper auxiliary function γ, it is possible to obtain the following reformulation of the estimation problem (10), suited to the finite element method (see Appendix B): find $(\hat{f} \circ X, \gamma \circ X) \in (H^1_{n0,\mathbf{K}}(\Omega) \cap C^0(\bar{\Omega})) \times H^1(\Omega)$ such that

$$\begin{aligned} &\boldsymbol{\mu}_n' \hat{\mathbf{f}}_n - \lambda \int_\Omega \mathbf{K} \nabla(\mu \circ X) \cdot \nabla(\gamma \circ X) d\Omega = \boldsymbol{\mu}_n' \mathbf{z} \\ &\int_\Omega (\xi \circ X)(\gamma \circ X) \mathcal{W} d\Omega + \int_\Omega \nabla(\xi \circ X) \mathbf{K} \nabla(\hat{f} \circ X) d\Omega = 0 \end{aligned} \tag{14}$$

for any $(\mu \circ X, \xi \circ X) \in (H^1_{n0,\mathbf{K}}(\Omega) \cap C^0(\bar{\Omega})) \times H^1(\Omega)$. Thanks to the regularity of the problem, $\hat{f} \circ X$ still belongs to $H^2_{n0,\mathbf{K}}(\Omega)$.

Using the finite element space $H^1_{\mathcal{T}}(\Omega)$, we consider the following discrete counterpart of this new estimation problem: find $(\hat{f} \circ X, \gamma \circ X) \in H^1_{\mathcal{T}}(\Omega) \times H^1_{\mathcal{T}}(\Omega)$ that satisfies (14) for any $(\mu \circ X, \xi \circ X) \in H^1_{\mathcal{T}}(\Omega) \times H^1_{\mathcal{T}}(\Omega)$, where the integrals are now computed over the domain triangulation $\Omega_{\mathcal{T}}$. Let us consider the mass and stiffness finite element matrices defined by

$$\mathbf{R}_0 = \int_{\Omega_{\mathcal{T}}} \boldsymbol{\psi} \boldsymbol{\psi}' \; \mathcal{W} d\Omega \qquad \text{and} \qquad \mathbf{R}_1 = \int_{\Omega_{\mathcal{T}}} \nabla \boldsymbol{\psi}' \mathbf{K} \nabla \boldsymbol{\psi} \; d\Omega,$$

respectively, with $\boldsymbol{\psi}$ defined as in (12). The integrals in (14) can be expressed as

$$\begin{aligned}
\int_{\Omega_{\mathcal{T}}} \mathbf{K}\nabla(\mu \circ X) \cdot \nabla(\gamma \circ X) d\Omega &= \boldsymbol{\gamma}'\mathbf{R}_1\boldsymbol{\mu} = \boldsymbol{\mu}'\mathbf{R}_1\boldsymbol{\gamma}, \\
\int_{\Omega_{\mathcal{T}}} (\xi \circ X)(\gamma \circ X)\mathcal{W} d\Omega &= \boldsymbol{\xi}'\mathbf{R}_0\boldsymbol{\gamma}, \\
\int_{\Omega_{\mathcal{T}}} \nabla(\xi \circ X)\mathbf{K}\nabla(\hat{f} \circ X) d\Omega &= \boldsymbol{\xi}'\mathbf{R}_1\hat{\mathbf{f}},
\end{aligned}$$

where $\boldsymbol{\xi}$, $\boldsymbol{\gamma}$, $\boldsymbol{\mu}$, $\hat{\mathbf{f}} \in \mathbb{R}^N$ are defined as in (12). Furthermore, we define the following block matrices:

$$\mathbf{L} = \begin{bmatrix} \mathbf{I}_n & \mathbf{O}_{n\times(N-n)} \\ \mathbf{O}_{(N-n)\times n} & \mathbf{O}_{(N-n)\times(N-n)} \end{bmatrix} \in \mathbb{R}^{N\times N} \text{ and } \mathbf{D} = \begin{bmatrix} \mathbf{I}_n \\ \mathbf{O}_{(N-n)\times n} \end{bmatrix} \in \mathbb{R}^{N\times n},$$

where $\mathbf{O}_{m_1\times m_2} \in \mathbb{R}^{m_1\times m_2}$ is the null matrix. These matrices allow us to express $\boldsymbol{\mu}_n'\hat{\mathbf{f}}_n = \boldsymbol{\mu}'\mathbf{L}\hat{\mathbf{f}}$ and $\boldsymbol{\mu}_n'\mathbf{z} = \boldsymbol{\mu}'\mathbf{L}\mathbf{D}\mathbf{z}$. Hence, the discrete counterpart of the estimation problem in (14) reduces to finding the pair of coefficient vectors $(\hat{\mathbf{f}}, \boldsymbol{\gamma}) \in \mathbb{R}^N \times \mathbb{R}^N$ such that, for any $(\boldsymbol{\mu}, \boldsymbol{\xi}) \in \mathbb{R}^N \times \mathbb{R}^N$, we have

$$\begin{cases} \boldsymbol{\mu}'\mathbf{L}\hat{\mathbf{f}} - \lambda\boldsymbol{\mu}'\mathbf{R}_1\boldsymbol{\gamma} = \boldsymbol{\mu}'\mathbf{L}\mathbf{D}\mathbf{z} \\ \boldsymbol{\xi}'\mathbf{R}_0\boldsymbol{\gamma} + \boldsymbol{\xi}'\mathbf{R}_1\hat{\mathbf{f}} = \mathbf{0}, \end{cases} \tag{15}$$

where $\mathbf{0} \in \mathbb{R}^N$ denotes the null vector. This leads to the following proposition.

Proposition 4.1 *The estimator $\hat{f} \circ X \in H^1_{\mathcal{T}}(\Omega)$ that solves the discrete counterpart of the estimation problem (14) is given by $\hat{f} \circ X = \hat{\mathbf{f}}'\boldsymbol{\psi}$, such that $\hat{\mathbf{f}}$ satisfies*

$$\begin{bmatrix} -\mathbf{L} & \lambda\mathbf{R}_1 \\ \lambda\mathbf{R}_1 & \lambda\mathbf{R}_0 \end{bmatrix} \begin{bmatrix} \hat{\mathbf{f}} \\ \boldsymbol{\gamma} \end{bmatrix} = \begin{bmatrix} -\mathbf{L}\mathbf{D}\mathbf{z} \\ \mathbf{0} \end{bmatrix}, \tag{16}$$

where $\boldsymbol{\gamma}$ is the vector associated with the auxiliary function γ in (14). Moreover $\hat{f} \circ X$ is uniquely determined.

In Appendix C, the uniqueness of the finite element solution to the estimation problem is proved by showing the invertibility of the matrices $\mathbf{R}_0$ and $\left(\mathbf{L} + \lambda\mathbf{R}_1\mathbf{R}_0^{-1}\mathbf{R}_1\right)$. By exploiting this fact, from (16) it follows that

$$\hat{\mathbf{f}} = \left(\mathbf{L} + \lambda\mathbf{R}_1\mathbf{R}_0^{-1}\mathbf{R}_1\right)^{-1}\mathbf{L}\mathbf{D}\mathbf{z}.$$

Note that the estimator is linear in the observed data $\mathbf{z}$ and has the typical penalized regression form, with the roughness penalty matrix $\mathbf{R}_1\mathbf{R}_0^{-1}\mathbf{R}_1$ accounting for the domain deformation implied by the flattening map via the matrices $\mathbf{R}_0$ and $\mathbf{R}_1$. Thanks to the linearity in the observed data values, classical inferential tools are available, such as approximate confidence bands for f and approximate prediction intervals at new data locations. Moreover, a closed form Generalized-Cross-Validation (GCV) criterion can be used to select the smoothing parameter λ. See Appendix D.

5 The covariate model

The inclusion of covariates in the proposed model can be obtained by extending the described framework to a semi-parametric model as in [23]. Let $\mathbf{w}_i = (w_{i1}, \ldots, w_{iq})$ be a q-vector of covariates associated with the variable of interest z_i observed at the location $\mathbf{x}_i$. We modify the model in (1) as

$$z_i = \mathbf{w}_i'\boldsymbol{\beta} + f(\mathbf{x}_i) + \epsilon_i, \qquad i = 1, \ldots, n, \tag{17}$$

where $\boldsymbol{\beta} \in \mathbb{R}^q$ is the vector of regression coefficients and the remaining terms are defined as in (1). To estimate $\boldsymbol{\beta}$ and f in (17), we now minimize the following penalized sum of squared error functional

$$J_{\Sigma,\lambda}(\boldsymbol{\beta}, f) = \sum_{i=1}^{n} \big(z_i - \mathbf{w}_i'\boldsymbol{\beta} - f(\mathbf{x}_i)\big)^2 + \lambda \int_\Sigma (\Delta_\Sigma f(\mathbf{x}))^2 \; d\Sigma.$$

Thus using the map X, we can consider the following equivalent estimation problem over the planar domain Ω: find $\boldsymbol{\beta} \in \mathbb{R}^q$ and $f \circ X \in H^2_{n0,\mathbf{K}}(\Omega)$ that minimize

$$J_{\Omega,\lambda}(\boldsymbol{\beta}, f \circ X) = \sum_{i=1}^{n} \big(z_i - \mathbf{w}_i'\boldsymbol{\beta} - f(X(\mathbf{u}_i))\big)^2 + \lambda \int_\Omega \frac{1}{\mathcal{W}} \bigg(\mathrm{div}(\mathbf{K}\nabla(f \circ X))\bigg)^2 d\Omega. \tag{18}$$

Let $\mathbf{W}$ be the $n \times q$ matrix whose i-th row is the vector $\mathbf{w}_i'$ of covariates associated with the i-th data location. We assume $\mathbf{W}$ has full rank. Define $\mathbf{P} = \mathbf{W}(\mathbf{W}'\mathbf{W})^{-1}\mathbf{W}'$ to be the matrix that orthogonally projects on the subspace of $\mathbb{R}^n$ spanned by the columns of $\mathbf{W}$. Let $\mathbf{Q} = (\mathbf{I}_n - \mathbf{P})$. Then the following corollary holds.

Corollary 1 *The estimators $\hat{\boldsymbol{\beta}}$ and $\hat{f} \circ X$ that minimize (18) over $\mathbb{R}^q$ and $H^2_{n0,\mathbf{K}}(\Omega)$, respectively are $\hat{\boldsymbol{\beta}} = (\mathbf{W}'\mathbf{W})^{-1}\mathbf{W}'(\mathbf{z} - \hat{\mathbf{f}}_n)$ and $\hat{f}$ that satisfies*

$$\boldsymbol{\mu}_n'\mathbf{Q}\hat{\mathbf{f}}_n + \lambda \int_\Omega \frac{1}{\mathcal{W}} \bigg(\mathrm{div}(\mathbf{K}\nabla(\mu \circ X))\bigg)\bigg(\mathrm{div}\Big(\mathbf{K}\nabla(\hat{f} \circ X)\Big)\bigg) d\Omega = \boldsymbol{\mu}_n'\mathbf{Q}\mathbf{z} \tag{19}$$

for any μ defined on Σ such that $\mu \circ X \in H^2_{n0,\mathbf{K}}(\Omega)$, with $\boldsymbol{\mu}_n$ and $\hat{\mathbf{f}}_n$ defined according to (9). Moreover, the estimators $\hat{\boldsymbol{\beta}}$ and $\hat{f} \circ X$ are uniquely determined.

The proof of this result follows by generalizing the proof of Proposition 3.1. In particular, an extra differentiation of the functional $J_{\Omega,\lambda}(\boldsymbol{\beta}, f \circ X)$ with respect to $\boldsymbol{\beta}$ has to be taken into account to obtain the minimizer $\hat{\boldsymbol{\beta}} = \hat{\boldsymbol{\beta}}(f)$. After plugging $\boldsymbol{\beta} = \hat{\boldsymbol{\beta}}$ into (18) the proof follows along the lines of Appendix A.

Following the same arguments invoked for the model in Section 2, an auxiliary function γ is introduced to derive the weak formulation of (19), analogous to (14). Hence the estimation problem is well suited for the discretization via a finite element space. By exploiting the matrices introduced in Section 4.3, except for the matrix $\mathbf{L}$ which is now replaced by

$$\tilde{\mathbf{L}} = \begin{bmatrix} \mathbf{Q} & \mathbf{O}_{n\times(N-n)} \\ \mathbf{O}_{(N-n)\times n} & \mathbf{O}_{(N-n)\times(N-n)} \end{bmatrix},$$

we obtain the following corollary.

Corollary 2 *The estimators* $\hat{\boldsymbol{\beta}} \in \mathbb{R}^q$ *and* $\hat{f} \circ X \in H^1_{\mathcal{T}}(\Omega)$ *that solve the discrete counterpart of the estimation problem with covariates are given by* $\hat{\boldsymbol{\beta}} = (\mathbf{W}'\mathbf{W})^{-1}\mathbf{W}'(\mathbf{z} - \hat{\mathbf{f}}_n)$ *and* $\hat{f} \circ X = \hat{\mathbf{f}}'\boldsymbol{\psi}$*, such that* $\hat{\mathbf{f}}$ *satisfies*

$$\begin{bmatrix} -\tilde{\mathbf{L}} & \lambda\mathbf{R}_1 \\ \lambda\mathbf{R}_1 & \lambda\mathbf{R}_0 \end{bmatrix} \begin{bmatrix} \hat{\mathbf{f}} \\ \boldsymbol{\gamma} \end{bmatrix} = \begin{bmatrix} -\tilde{\mathbf{L}}\mathbf{D}\mathbf{z} \\ \mathbf{0} \end{bmatrix}, \tag{20}$$

where $\boldsymbol{\gamma}$ *is the vector associated with the auxiliary function* γ*. Moreover* $\hat{\boldsymbol{\beta}}$ *and* $\hat{f} \circ X$ *are uniquely determined.*

The estimators $\hat{\boldsymbol{\beta}}$ and $\hat{\mathbf{f}}$ are linear in the observed data values $\mathbf{z}$. Some distributional properties are reported in Appendix D.

6 Simulations studies

In this section, we present the results of some simulations to illustrate the performance of the proposed technique on a variety of non-planar domains. In particular, we compare three methods: the proposed Spatial Regression models over Non-Planar domains[1] (SR-NP), the Spatial Regression models over Planar domains (SR-P) introduced in [22] and [23], and Iterative Heat Kernel smoothing (IHK) described in [6]. Since IHK is not currently designed for the inclusion of covariates, the simulations provided here do not include covariates. The three methods are compared on four different tubular domains: in particular, three are test domains while the fourth one coincides with a real-geometry from the AneuRisk dataset (see Figure 6). Notice that the selected AneuRisk geometry does not present an aneurysm.

To implement the SR-P models, we first flatten the original non-planar domain via the angular flattening map used in [4] for the analysis of the AneuRisk data. To obtain the angular map, we start by computing the centerline of the tubular domain. Then, each point (x_1, x_2, x_3) on the non-planar domain Σ is associated with the closest point on the centerline. Hence, it is possible to consider the cylindrical parametrization defined by (s, r, θ), where s is the curvilinear abscissa computed along the centerline, r is the artery radius (i.e., the distance between (x_1, x_2, x_3) and the associated centerline point), and θ is the angle in radians identified by (x_1, x_2, x_3) with respect to the curvilinear abscissa. The

[1]The proposed model has been implemented in R [20] and Matlab. Both versions will be shortly released.

angular map thus takes Σ to the rectangle $(s, \theta\bar{r})$, where $\bar{r}$ is the average radius. Analogous to [4], the necessary $(2\pi\bar{r})-$periodicity of the estimate along the coordinate $\theta\bar{r}$, is obtained by augmenting the data with repeated data values, at the same abscissas but with ordinates given by $(\theta+2\pi)\bar{r}$ and $(\theta-2\pi)\bar{r}$, respectively. Recall that the angular map excludes the aneurysmal sac (otherwise multiple points on the wall of the carotid artery may be mapped to the same point on the plane). This remark justifies the choice made for the real-geometry in Figure 6. Moreover, being designed for planar domains, the SR-P model uses the standard Laplacian of the function in the penalty term and thus the information about the geometry of the original three-dimensional domain is lost. Finally, the optimal value of the smoothing parameter λ for SR-P is selected at each simulation replicate and each domain by GCV. The same criterion used to select λ for the proposed SR-NP approach (see Appendix D for the details on GCV).

Iterative heat kernel smoothing has been developed for neuroimaging applications, to deal with very complex domain geometries such as the cortical surface of the brain, which is usually approximated by three-dimensional meshes with more than 10^6 nodes. The purpose of the iterative nature of the IHK algorithm is to reduce the computational burden associated with such geometries. In particular, IHK works directly on the mesh without any flattening. To do this, the Laplace-Beltrami eigenvalue problem is solved directly on the surface Σ, i.e., ordered eigenvalues $0 = \lambda_0 \leq \lambda_1 \leq \lambda_2 \leq \cdots$ and the corresponding eigenfunctions $\phi_0, \phi_1, \phi_2, \ldots$ are found by solving $-\Delta_\Sigma \phi_j = \lambda \phi_j$ on Σ. Thus the heat kernel with bandwidth t is constructed from the eigenvalue-eigenfunction pairs $\{(\lambda_j, \phi_j)\}$ as $K_t(p, q) = \sum_{j=0}^{\infty} e^{-\lambda_j t} \phi_j(p)\phi_j(q)$, where p and q are two generic points on Σ. The heat kernel smoothing of z_i is given by $K_t * z_i = \sum_{j=0}^{\infty} e^{-\lambda_j t} \beta_j \phi_j(\mathbf{x}_i)$, where $\beta_j(\mathbf{x}_i) = \langle z_i, \phi_j \rangle$. In practice, only k eigenvalue-eigenfunction pairs are chosen via an iterative residual fitting algorithm. For our simulations, we made a heuristic choice by selecting the bandwidth with the best performance after some test runs. In particular, we set $t = 10^{-3}$. To determine the level of smoothing, the optimal number of iterations is selected for each simulation replicate and each domain via the F-test criterium outlined in [6].

We generate simulation data as follows. Over each non-planar test domain, we consider fifty test functions, having the form

$$f(x_1, x_2, x_3) = a_1 \sin(2\pi x_1) + a_2 \sin(2\pi x_2) + a_3 \sin(2\pi x_3) + 1, \tag{21}$$

with coefficients a_j, for $j = 1, 2, 3$, randomly generated from independent normal distributions with mean one and standard deviation one. For each geometry, the data locations $\mathbf{x}_i$, for $i = 1, \ldots, n$, coincide with the nodes of the three-dimensional mesh used to approximate the domain (see, e.g., Figure 4 (left) for the triangular mesh approximating Geometry 2). Noisy data values are obtained, in accordance with the model (1), by adding independent normally distributed errors with mean zero and a standard deviation 0.5 to each of the data locations. Figure 6 illustrates, for each geometry considered, (top) an example

MSE	Geometry 1	Geometry 2	Geometry 3	Geometry 4
SR-NP	0.0188(0.0103)	0.077(0.0889)	0.0644(0.0512)	0.0145(0.0074)
SR-P	0.0252(0.0157)	0.140(0.1230)	0.0730(0.0572)	0.0187(0.0174)
IHK	0.0459(0.0128)	0.061(0.0774)	0.1350(0.1660)	0.0354(0.0431)

Table 1: Median (inter-quantile ranges) of MSEs for the estimators of f associated with the three approaches.

Wilcoxon tests	Geometry 1	Geometry 2	Geometry 3	Geometry 4
SR-NP vs. SR-P	3.895×10^{-10}	3.895×10^{-10}	2.202×10^{-3}	7.548×10^{-8}
SR-NP vs. IHK	3.895×10^{-10}	8.022×10^{-1}	3.895×10^{-10}	8.032×10^{-10}

Table 2: P-values of the pairwise Wilcoxon tests verifying that the distribution of MSEs of the estimators provided by SR-NP is stochastically lower than the distribution of MSEs of the estimators provided by the other methods.

of a test function generated by (21), (middle) the corresponding level of noise and (bottom) the associated SR-NP estimate. The color maps are obtained by linear interpolation of the data at $\mathbf{x}_i$. In particular, we have employed Matlab code made available by M. Chung et al. (see [6] for more details). The good properties of the proposed estimator are evident from the results in the last row, where the estimates for all the geometries are of good quality despite the presence of noise.

For each simulation replicate and test domain, we compute the Mean Square Error (MSE) of the estimator associated with each of the three different methods. Figure 7 shows the box plots of the MSEs and Table 1 reports the corresponding medians and inter-quantile ranges over the fifty simulation replicates. The box plots show that, in most cases, the SR-NP model yields better estimates with a smaller variance. This notion is explored quantitatively in Table 2 which reports the results of pairwise Wilcoxon tests verifying that the distribution of MSEs for the SR-NP estimators are stochastically lower than the corresponding distribution for the SR-P and IHK estimators. The p-values of these tests show that the MSEs of SR-NP is significantly lower than the ones of SR-P, uniformly over the four test domains. These results highlight the advantages of the proposed spatial regression model over non-planar domains with respect to the corresponding methodology applied over planar domains; i.e., accounting for the geometry of the non-planar domain leads to significantly improved estimates. The values in Tables 1 and 2 also show that the proposed SR-NP model yields significantly better estimates than IHK for three of the geometries considered. For Geometry 2, in fact, IHK has a lower median MSE than SR-NP. However, when the converse Wilcoxon test is applied, i.e., with the alternative that the distribution of the MSEs for IHK is stochastically lower than the corresponding distribution of the MSEs for SR-NP, we attain a p-value of 0.2005. Hence for Geometry 2, these two methods are in fact competitive. Notice that we are applying IHK to simpler geometries than the ones for which it has been designed and optimized. Hence the simulations show that within the scope of the geometries characteriz-

Figure 6: Top: an example of a test function generated by (21) on four tubular domains; the fourth is a real geometry of an internal carotid artery from the AneuRisk dataset. Middle: Data with noise. Bottom: estimates proved by SR-NP.

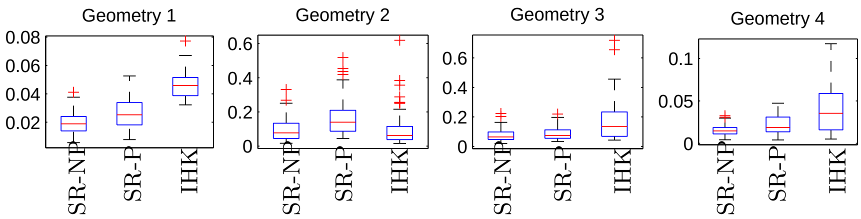

Figure 7: Box plots of the MSEs for the three estimators over the fifty simulations.

ing our application, the proposed SR-NP method has a competitive advantage. In future work, we will test our method on more complex geometries, such as the ones characterizing the cortical surface of the brain.

6.1 Hemodynamic data

In this section, we present the application to the AneuRisk data. The AneuRisk project[2] gathered researchers of different scientific fields, ranging from neurosurgery and neuroradiology to statistics, numerical analysis and bio-engineering, with the aim of studying the pathogenesis of cerebral aneurysms. Aneurysms are deformations of the vessel wall. Their formation is usually ascribed to the complex interplay between the biomechanical properties of artery walls and the effects of hemodynamic forces exerted on the vessel walls, such as wall shear stress and pressure. The hemodynamic forces in turn depend on the vessel morphology itself. While the first studies on the aneurysmal pathology restricted their attention to the aneurysmal sac, the AneuRisk project also investigated the morphological and hemodynamic features of the parent vasculature, i.e., of the vessel hosting the aneurysm and the upstream vasculature, with the goal of highlighting possible causes of aneurysm onset, development and rupture (see [17], [24] and the references therein).

Here, we analyze hemodynamic data on a real internal carotid artery. In particular, the hemodynamic quantities of interest such as wall shear stress and pressure, are computed via computational fluid dynamics simulations over the real anatomy (see [16]). The inner carotid artery geometry is generated via the reconstruction algorithm coded in the Vascular Modeling ToolKit (VMTK) from three-dimensional angiographic images, belonging to the AneuRisk data warehouse (see, e.g., [18]). Figure 1 shows the modulus of the simulated wall

[2]The project involved MOX Laboratory for Modeling and Scientific Computing (Dip. di Matematica, Politecnico di Milano), Laboratory of Biological Structure Mechanics (Dip. di Ingegneria Strutturale, Politecnico di Milano), Istituto Mario Negri (Ranica), Ospedale Niguarda Ca' Granda (Milano) and Ospedale Maggiore Policlinico (Milano), and has been supported by Fondazione Politecnico di Milano and Siemens Medical Solutions Italia. More information about the project can be found at the AneuRisk webpage http://mox.polimi.it/it/progetti/aneurisk/.

shear stress at the systolic peak on a three-dimensional geometry.

According to the approach in this paper, the three-dimensional triangular mesh in Figure 2 approximating the artery is flattened via the conformal map described in Section 4.2 to create the planar triangulation in Figure 8. The sides of the planar triangulation are labeled in correspondence with Figure 2. In particular, the sides of the planar triangulation labeled with “inflow” and “outflow” correspond to the open ends of the carotid artery. The sides indicated by “cut” correspond to a longitudinal cut along the artery wall, connecting the open boundaries of the artery. The aneurysm and major curves of the artery are also recognizable in the flattened domain. The area of the mesh which is very fine and close to the “outflow” side corresponds to the aneurysmal sac.

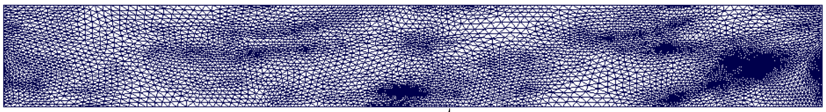

Figure 8: Planar triangulation generated by the conformal flattening of the mesh in Figure 2 approximating the internal carotid artery in Figure 1.

Figure 9 (left) shows the smoothed values for the modulus of the wall shear stress obtained via the SR-NP approach with smoothing parameter $\lambda = 10^{1.5}$. In the bottom part of the picture, the estimated wall shear stress is plotted over the equivalent planar domain, a byproduct of the proposed method. This planar view of the data is very practical since it allows us to see the entire geometry without rotating the figure, thus making areas of interest easier to highlight. We recognize large areas of high wall shear stress, in correspondence with the neck of the aneurysm and along the first major bend of the carotid syphon. This highlights the sensitivity of the wall shear stress on the complexity of the geometry of the artery.

Figure 9 (right) displays some preliminary results where we explore the relationship between the wall shear stress and some geometrical features of the artery. In particular, we consider local curvature of the vessel wall, the curvature of the artery centerline and local radius of the vessel. The local curvature of the vessel wall is calculated from the three-dimensional mesh as in [13] and varies between -20.63 cm^{-1} and 36.46 cm^{-1}. The curvature of the vessel centerline identifies the curvature of the whole vascular geometry. The artery centerline and its curvature are computed as described in [25]. In particular, to measure the centerline curvature at each point on the vessel wall we refer to the curvature at an associated centerline point. The centerline curvature varies from 0.05 cm^{-1} and 4.64 cm^{-1}. Finally, the local radius of the vessel is measured as the distance from the artery wall to the associated centerline point and ranges from 0.14 cm to 0.43 cm. All three covariates are significant for the model

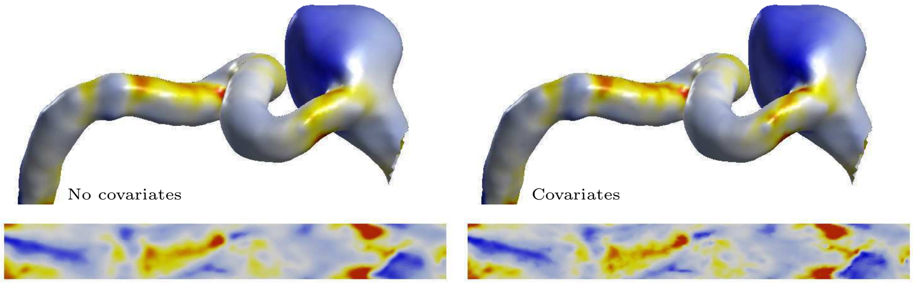

Figure 9: Estimates of the wall shear stress modulus obtained with the SR-NP approach without including any covariates (left) and by including covariates (right). The colormap on both plots ranges from 0 (blue) to 200 (red).

at hand, with estimated parameters $\hat{\boldsymbol{\beta}} = (-0.9874,\ 0.3545,\ -78.3395)'$, with smoothing parameter $\lambda = 10^{0.5}$. Hence, local wall curvature and local radius are negatively associated with the wall shear stress, while the artery centerline curvature is positively associated. The most influential contributor to the wall shear stress appears to be the local radius, as expected. These preliminary studies will be further investigated in a future work, with statistical analysis across patients. Using the SR-NP method, patient-specific estimates can all be mapped into a common planar domain where, after suitable registration among patients, comparisons across patients can be made. These analyses aim at highlighting recurrent hemodynamic patterns and relate them to the presence and the location of aneurysms.

7 Future developments

Among our future goals, we are going to extend the proposed model to include a time dimension. For instance, it could be of great interest to repeat the analysis in Section 6.1 performed as the systolic peak to the whole cardiac cycle to investigate the oscillations of the wall shear stress. We are interested in two different approaches to tackle this problem. We can consider these data as surfaces evolving in time, and hence generalize the proposed method by considering time-dependent differential operators. Or, alternatively, we can represent these data as space-dependent curves, where at each data location we consider the temporal profile of the variable of interest. This would lead us to extend the proposed model to the case of functional responses.

Other possible generalizations, that broaden the application potential of the proposed method, include the case of general link functions such as the logit, and loss-functions other than the classical sum of squared errors. Moreover, the model could be extended to a full functional regression setting where the covariates are modeled as surfaces. By considering different flattening methods, the model could be extended to applications involving other types of Riemannian manifolds.

Another promising line of research consists in the generalization of the SR-NP approach to other differential operators, still defined on non-planar domains. The objective in this extension is twofold. First, following the rationale in [1], we might modify the penalty term with a differential operator that includes a priori knowledge on the phenomenon at hand. Secondly, the penalty term might be used to target some specific quantities of interest in accordance with a so-called goal-orientated approach [2].

On the computational side, there is a possibility to solve the estimation problem in (2) directly on the non-planar domain, without resorting to a flattening map. This would probably lead to a computational saving, although mapping the estimates to a reference domain may still be of interest, allowing for more direct comparisons across different geometries.

References

[1] L. Azzimonti, L. M. Sangalli, P. Secchi, S. Romagnoli, and M. Domanin. Pde penalization for spatial fields smoothing. In *Proceedings of SIS Scientific Meeting 2012, 46th Scientific Meeting of the Italian Statistical Society*, 2012.

[2] W. Bangerth and R. Rannacher. *Adaptive finite element methods for differential equations*. Birkhauser Verlag, Basel, 2003.

[3] V. Baramidze, M. J. Lai, and C. K. Shum. Spherical splines for data interpolation and fitting. *SIAM J. Scientific Computing*, 28:241–259, 2006.

[4] A. Boneschi. Functional data analysis of CFD simulations: the systolic wall shear stress map of the internal carotid artery. Master's thesis, Politecnico di Milano, Milano, 2012. available at http://mox.polimi.it/it/progetti/pubblicazioni/tesi/boneschi.pdf.

[5] D. Braess. *Finite Elements: Theory, Fast Solvers, and Applications in Solid Mechanics*. Cambridge University Press, New York, NY, 2 edition, 2007.

[6] Moo K. Chung, Steven M. Robbins, Kim M. Dalton, Richard J. Davidson, Andrew L. Alexander, and Alan C. Evans. Cortical thickness analysis in autism with heat kernel smoothing. *NeuroImage*, 25:1256–1265, 2005.

[7] Ph. Ciarlet. *The Finite Element Method for Elliptics Problems*. North-Holland, Amsterdam, 1978.

[8] Ulrich Dierkes, Stefan Hildebrandt, and Friedrich Sauvigny. *Minimal Surfaces*, volume 1. Springer, Heidelberg, 2 edition, 2010.

[9] F. Ferraty and P. Vieu. *Nonparametric Functional Data Analysis: Theory and Practice*. Springer Series in Statistics. Springer-Verlag, London, 2006.

[10] Christophe Geuzaine and J. F. Remacle. *Gmsh Reference Manual*. (http://www.geuz.org/gmsh), 1.12 edition, August 2003.

[11] D. J. Hagler, Jr., A. P. Saygin, and M. I. Sereno. Smoothing and cluster thresholding for cortical surface-based group analysis of fMRI data. *NeuroImage*, 33:1093–1103, 2006.

[12] S. Haker, S. Angenent, A. Tannenbaum, and R. Kikinis. Nondistorting flattening maps and the 3-D visualization of colon CT images. *IEEE Trans. Med. Imag.*, 19:665–670, 2000.

[13] J. Ole Kaven. *Curvature calculations on triangular 3D surface*. http://www.mathworks.com/matlabcentral/fileexchange/authors/33868, August 2009.

[14] F. Lindgren, H. Rue, and J. Lindström. An explicit link between gaussian fields and gaussian markov random fields: the stochastic partial differential equation approach. *J. R. Statist. Soc. Ser. B*, 73:423–498, 2011. with discussions and a reply by the authors.

[15] J.-L. Lions and E. Magenes. *Non-Homogeneous Boundary Value Problems and Applications*, volume III. Springer-Verlag, New York, 1973.

[16] T. Passerini. *Computational Hemodynamics of the Cerebral Circulation: Multiscale Modeling from the Circle of Willis to Cerebral Aneurysms*. PhD thesis, Dipartimento di Matematica, Politecnico di Milano, Italy, 2009. available at http://mathcs.emory.edu/.

[17] T. Passerini, L. M. Sangalli, S. Vantini, M. Piccinelli, S. Bacigaluppi, L. Antiga, E. Boccardi, P. Secchi, and A. Veneziani. An integrated cfd-statistical investigation of parent vasculature of cerebral aneurysms. *Cardio. Eng. and Tech.*, 3(1):26–40, 2012.

[18] M. Piccinelli, A. Veneziani, D.A. Steinman, A. Remuzzi, and L. Antiga. A framework for geometric analysis of 852 vascular structures: applications to cerebral aneurysms. *IEEE Trans. Med. Imag.*, 28(8):1141–1155, 2009.

[19] Ulrich Pinkall and Konrad Polthier. Computing discrete minimal surfaces and their conjugates. *Experimental Mathematics*, 2:15–36, 1993.

[20] R Core Team. *R: A Language and Environment for Statistical Computing*. R Foundation for Statistical Computing, Vienna, Austria, 2012. ISBN 3-900051-07-0.

[21] J. Ramsay and B. W. Silverman. *Functional Data Analysis*. Springer-Verlag, New York, 2 edition, 2005.

[22] Tim Ramsay. Spline smoothing over difficult regions. *J. R. Statist. Soc. Ser. B*, 64(2):307–319, 2002.

[23] L. M. Sangalli, J. O. Ramsay, and T. O. Ramsay. Spatial spline regression models. *J. R. Statist. Soc. Ser. B*, 2012. To appear, available at http://mox.polimi.it/it/progetti/pubblicazioni/.

[24] L. M. Sangalli, P. Secchi, S. Vantini, and A. Veneziani. A case study in exploratory functional data analysis: geometrical features of the internal carotid artery. *J. Am. Stat. Assoc.*, 104(485):37–48, 2009.

[25] L. M. Sangalli, P. Secchi, S. Vantini, and A. Veneziani. Efficient estimation of three-dimensional curves and their derivatives by free-knot regression splines, applied to the analysis of inner carotid artery centrelines. *J. R. Statist. Soc. Ser. C*, 58:285–306, 2009.

[26] H. Wang and J. S. Marron. Object oriented data analysis: sets of trees. *Ann. Statist.*, 35:1849–1873, 2007.

A Proof of Proposition 3.1

For the proof, we need the following characterization theorem from Chapter 2 of [5].

Lemma A.1 *Let $\mathcal{A}$ be a symmetric coercive bilinear form on a vector space V and $\mathcal{B}$ a linear form on V. Then there exists in V a minimizer ξ of the form $\mathcal{A}(y,y) - 2\mathcal{B}(y)$, for $y \in V$, if and only if $\mathcal{A}(\xi, y) = \mathcal{B}(y)$, for any $y \in V$. Moreover, the minimizer ξ is unique.*

Now, we write the functional in (5) as

$$J_{\Omega,\lambda}(f \circ X) = \mathbf{z}'\mathbf{z} - 2\mathbf{f}_n'\mathbf{z} + \mathbf{f}_n'\mathbf{f}_n + \lambda \int_\Omega \frac{1}{\mathcal{W}} \Big(\mathrm{div}(\mathbf{K}\nabla(f \circ X))\Big)^2 d\Omega.$$

Since we are solving the optimization problem with respect to $f \circ X$, we can ignore the terms that are constant with respect to $f \circ X$ and look for a solution $f \circ X \in H^2_{n0,\mathbf{K}}(\Omega)$ that minimizes

$$\tilde{J}_{\Omega,\lambda}(f \circ X) = \left[\mathbf{f}_n'\mathbf{f}_n + \lambda \int_\Omega \frac{1}{\mathcal{W}} \Big(\mathrm{div}(\mathbf{K}\nabla(f \circ X))\Big)^2 d\Omega\right] - 2\mathbf{f}_n'\mathbf{z}.$$

To minimize $\tilde{J}_{\Omega,\lambda}(f \circ X)$, we apply Lemma A.1 with $V = H^2_{n0,\mathbf{K}}(\Omega)$, $\mathcal{B}(y) = \boldsymbol{y}_n'\mathbf{z}$, and

$$\mathcal{A}(f \circ X, y \circ X) = \boldsymbol{y}_n'\mathbf{f}_n + \lambda \int_\Omega \frac{1}{\mathcal{W}} \Big(\mathrm{div}(\mathbf{K}\nabla(f \circ X))\Big)\Big(\mathrm{div}(\mathbf{K}\nabla(y \circ X))\Big) d\Omega.$$

To show that the above bilinear form is coercive, we suppose that $\mathcal{A}(f \circ X, f \circ X) = 0$ for some $f \circ X \in H^2_{n0,\mathbf{K}}(\Omega)$. Then, we have $\mathbf{f}_n'\mathbf{f}_n = 0$ and

$$\int_\Omega \frac{1}{\mathcal{W}} \Big(\mathrm{div}(\mathbf{K}\nabla(f \circ X))\Big)^2 d\Omega = 0,$$

where $\mathcal{W}$ is positive and the matrix $\mathbf{K}$ is positive definite. The boundary conditions imposed on the co-normal derivatives in $H^2_{n0,\mathbf{K}}(\Omega)$ force $f \circ X$ to be a constant on Ω. Moreover, the condition $\mathbf{f}_n'\mathbf{f}_n = 0$ implies that $f \circ X$ is the constant null function on Ω. Thus $\mathcal{A}$ is coercive on $H^2_{n0,\mathbf{K}}(\Omega)$ and via Lemma A.1, the function $\hat{f} \circ X$ is the unique minimizer of (5) in $H^2_{n0,\mathbf{K}}(\Omega)$ if and only if $\hat{f} \circ X$ satisfies (10).

B Weak formulation of the estimation problem

To obtain an equivalent formulation for (10) suited for a finite element approximation, we introduce an auxiliary function γ defined on Σ. Then, the problem of finding $\hat{f}$ defined on Σ such that $\hat{f} \circ X \in H^2_{n0,\mathbf{K}}(\Omega)$ satisfies (10) for any μ on Σ where $\mu \circ X \in H^2_{n0,\mathbf{K}}(\Omega)$, can be rewritten as the problem of finding a pair of functions $\hat{f}$ and γ such that $(\hat{f} \circ X, \gamma \circ X) \in H^2_{n0,\mathbf{K}}(\Omega) \times L^2(\Omega)$ and satisfies

$$\begin{aligned} &\boldsymbol{\mu}_n' \hat{\mathbf{f}}_n + \lambda \int_\Omega (\gamma \circ X) \ \mathrm{div}(\mathbf{K}\nabla(\mu \circ X))\, d\Omega = \boldsymbol{\mu}_n' \mathbf{z} \\ &\int_\Omega (\gamma \circ X)(\xi \circ X) \mathcal{W} d\Omega - \int_\Omega \mathrm{div}\Big(\mathbf{K}\nabla(\hat{f} \circ X)\Big)\, (\xi \circ X) d\Omega = 0 \end{aligned} \tag{22}$$

for any $(\mu \circ X, \xi \circ X) \in H^2_{n0,\mathbf{K}}(\Omega) \times L^2(\Omega)$. If the pair $(\hat{f} \circ X, \gamma \circ X) \in H^2_{n0,\mathbf{K}}(\Omega) \times L^2(\Omega)$ satisfies (22) for any $(\mu \circ X, \xi \circ X) \in H^2_{n0,\mathbf{K}}(\Omega) \times L^2(\Omega)$, then $\hat{f} \circ X$ also satisfies (10). Of course, if $\hat{f} \circ X$ satisfies (10) then the pair $(\hat{f} \circ X\ ,\ \mathrm{div}(\mathbf{K}\nabla(f \circ X)))$ satisfies (22). Now, we ask for higher regularity of the auxiliary function γ and the test function ξ, i.e., $\gamma \circ X, \xi \circ X \in H^1(\Omega)$. With the added regularity and by exploiting Green's Theorem, problem (22) can be reformulated as finding $(\hat{f} \circ X, \gamma \circ X) \in (H^1_{n0,\mathbf{K}}(\Omega) \cap C^0(\bar{\Omega})) \times H^1(\Omega)$ such that (14) is verified for any $(\mu \circ X, \xi \circ X) \in (H^1_{n0,\mathbf{K}}(\Omega) \cap C^0(\bar{\Omega})) \times H^1(\Omega)$. Moreover, the elliptic regularity property ensures that $\hat{f} \circ X$ still belongs to $H^2_{n0}(\Omega)$ [see, e.g., 15, Chapter 8].

C Uniqueness of the finite element solution to the estimation problem

To show that the matrix $\left(\mathbf{L} + \lambda \mathbf{R}_1 \mathbf{R}_0^{-1} \mathbf{R}_1\right)$ is invertible, we show that it is symmetric positive definite. First note, $\mathbf{R}_0$ is symmetric positive definite since it coincides with a mass matrix weighted by a strictly positive quantity $\mathcal{W}$. The matrix $\mathbf{R}_0^{-1}$ is also symmetric positive definite. A similar argument holds for the symmetric positive definiteness of $\mathbf{R}_1$. By definition $\mathbf{L}$ is symmetric positive-semidefinite. Hence we know that $\left(\mathbf{L} + \lambda \mathbf{R}_1 \mathbf{R}_0^{-1} \mathbf{R}_1\right)$ is at least positive semi-definite. Suppose that $\mathbf{c}' \left(\mathbf{L} + \lambda \mathbf{R}_1 \mathbf{R}_0^{-1} \mathbf{R}_1\right) \mathbf{c} = 0$ for some $\mathbf{c} \in \mathbb{R}^N$. Then

$$0 = \mathbf{c}' \left(\mathbf{L} + \lambda \mathbf{R}_1 \mathbf{R}_0^{-1} \mathbf{R}_1\right) \mathbf{c} = \mathbf{c}'\mathbf{L}\mathbf{c} + \lambda \mathbf{c}' \mathbf{R}_1 \mathbf{R}_0^{-1} \mathbf{R}_1 \mathbf{c}$$

where both terms in the sum are non-negative. So it follows that $\mathbf{c}'L\mathbf{c} = 0$ and $\mathbf{c}'\mathbf{R}_1\mathbf{R}_0^{-1}\mathbf{R}_1\mathbf{c} = 0$. The positive definiteness of $\mathbf{R}_0^{-1}$ implies that $\mathbf{R}_1\mathbf{c} = 0$ or, specifically, that

$$0 = \mathbf{c}'\mathbf{R}_1\mathbf{c} = \int_{\Omega_\mathcal{T}} \mathbf{c}' \left(\nabla \boldsymbol{\psi}' \mathbf{K} \nabla \boldsymbol{\psi}\right) \mathbf{c}\ d\Omega = \int_{\Omega_\mathcal{T}} (\nabla \boldsymbol{\psi} \mathbf{c})' \mathbf{K} \nabla \boldsymbol{\psi} \mathbf{c}\ d\Omega = \|\nabla \boldsymbol{\psi} \mathbf{c}\|^2_{\mathbf{K}}$$

where $\|\mathbf{y}\|_{\mathbf{K}} = \sqrt{\mathbf{y}'\mathbf{K}\mathbf{y}}$ is the $\mathbf{K}$-norm for a generic vector $\mathbf{y} \in \mathbb{R}^N$. Now, the finite element expansion (11) yields

$$\nabla \boldsymbol{\psi} \mathbf{c} = \sum_{j=1}^N c_j \nabla \psi_j(\mathbf{x}) = \nabla \sum_{j=1}^N c_j \psi_j(\mathbf{x}) = \nabla(\mathbf{c}'\boldsymbol{\psi}),$$

where c_j's are the nodal values of the finite element function $\mathbf{c}'\boldsymbol{\psi}$. Since $\|\nabla \boldsymbol{\psi} \mathbf{c}\|^2_{\mathbf{K}} = 0$, we have that $\mathbf{c}'\boldsymbol{\psi}$ is a constant function. Since $\mathbf{c}'L\mathbf{c} = 0$, we have that $\mathbf{c} = \mathbf{0}$. Thus proving $\left(\mathbf{L} + \lambda \mathbf{R}_1 \mathbf{R}_0^{-1} \mathbf{R}_1\right)$ is positive definite.

D Properties of the estimators

In this section, we provide some properties of the proposed estimators. We start with the model without covariates. Let $\mathbf{B}$ denote the matrix on the lefthand side of (16) and set $\mathbf{A} = -\mathbf{B}^{-1}$.

We denote by $\mathbf{A}_n$ the submatrix given by the first n rows and n columns of $\mathbf{A}$ and by $\mathbf{A}_{Nn}$ the submatrix constituted by the first N rows and n columns of $\mathbf{A}$. In matrix form, the estimators are expressed as $\hat{\mathbf{f}}_n = \mathbf{A}_n\mathbf{z}$ and $\hat{\mathbf{f}} = \mathbf{A}_{Nn}\mathbf{z} = \mathbf{A}_{Nn}\mathbf{A}_n^{-1}\hat{\mathbf{f}}_n$. Note that the finite element solution $\hat{\mathbf{f}}$ is identified by $\hat{\mathbf{f}}_n$, i.e., by the solution at the n data locations $\mathbf{x}_i$. Furthermore, we have

$$E[\hat{\mathbf{f}}_n] = \mathbf{A}_n\mathbf{f}_n \qquad \text{and} \qquad Var(\hat{\mathbf{f}}_n) = \sigma^2\mathbf{A}_n\mathbf{A}_n. \tag{23}$$

The vector of fitted values at the n data locations is given by $\hat{\mathbf{z}} = \hat{\mathbf{f}}_n = \mathbf{A}_n\mathbf{z}$, yielding $\mathbf{S} = \mathbf{A}_n$ as the smoothing matrix. To measure the equivalent degrees of freedom for a linear estimator, we use the trace of the smoothing matrix. Hence we can estimate σ^2 by $\hat{\sigma}^2 = (\mathbf{z}-\hat{\mathbf{z}})'(\mathbf{z}-\hat{\mathbf{z}})/(n - tr(\mathbf{S}))$ where $tr(\mathbf{S})$ denotes the trace of the matrix $\mathbf{S}$. This estimate of σ, in combination with the variance expression in (23), can be used to derive approximate confidence bands for f. Moreover, the smoothing parameter λ is selected by Genearlized-Cross-Validation, i.e., $GCV(\lambda) = (\mathbf{z}-\hat{\mathbf{z}})'(\mathbf{z}-\hat{\mathbf{z}})/(n(1-tr(\mathbf{S})/n)^2)$. The predicted value of a new observation at $\mathbf{x}_{n+1}$ is given by evaluating the finite element solution at the data new data location, i.e., $\hat{z}_{n+1} = \hat{\mathbf{f}}'\boldsymbol{\psi}(\mathbf{u}_{n+1})$, where $X(\mathbf{u}_{n+1}) = \mathbf{x}_{n+1}$. The mean and variance of $\hat{z}_{n+1}$ can be obtained from (23) and approximate prediction intervals may be derived.

For the model with covariates, let $\widetilde{\mathbf{B}}$ denote the matrix on the lefthand side of (20) and likewise set $\widetilde{\mathbf{A}} = -\widetilde{\mathbf{B}}^{-1}$, $\widetilde{\mathbf{A}}_n$ and $\widetilde{\mathbf{A}}_{Nn}$ according to the definitions above. Then, $\hat{\mathbf{f}}_n = \widetilde{\mathbf{A}}_n\mathbf{Q}\mathbf{z}$, $\hat{\mathbf{f}} = \widetilde{\mathbf{A}}_{Nn}\mathbf{Q}\mathbf{z} = \widetilde{\mathbf{A}}_{Nn}\widetilde{\mathbf{A}}_n^{-1}\hat{\mathbf{f}}_n$, and $\hat{\boldsymbol{\beta}} = (\mathbf{W}'\mathbf{W})^{-1}\mathbf{W}'(\mathbf{I}-\widetilde{\mathbf{A}}_n\mathbf{Q})\mathbf{z}$. Thus, with some algebra, we derive

$$\begin{aligned} &E[\hat{\mathbf{f}}_n] = \widetilde{\mathbf{A}}_n\mathbf{Q}\mathbf{f}_n, && E[\hat{\boldsymbol{\beta}}] = \boldsymbol{\beta} + (\mathbf{W}'\mathbf{W})^{-1}\mathbf{W}'(\mathbf{I}-\widetilde{\mathbf{A}}_n\mathbf{Q})\mathbf{f}_n,\\ &Var(\hat{\mathbf{f}}_n) = \sigma^2\widetilde{\mathbf{A}}_n\mathbf{Q}\widetilde{\mathbf{A}}_n, && Var(\hat{\boldsymbol{\beta}}) = \sigma^2(\mathbf{W}'\mathbf{W})^{-1} + \sigma^2(\mathbf{W}'\mathbf{W})^{-1}\mathbf{W}'(\widetilde{\mathbf{A}}_n\mathbf{Q}\widetilde{\mathbf{A}}_n)\mathbf{W}(\mathbf{W}'\mathbf{W})^{-1}. \end{aligned}$$

The vector of fitted values at the n data locations is given by $\hat{\mathbf{z}} = \mathbf{W}\hat{\boldsymbol{\beta}} + \hat{\mathbf{f}}_n = (\mathbf{P}+\mathbf{Q}\widetilde{\mathbf{A}}_n\mathbf{Q})\mathbf{z} = \widetilde{\mathbf{S}}\mathbf{z}$ where the smoothing matrix is $\widetilde{\mathbf{S}} = \mathbf{P}+\mathbf{Q}\widetilde{\mathbf{A}}_n\mathbf{Q}$. The equivalent degrees of freedom of this model are thus given by $tr(\widetilde{\mathbf{S}}) = q + tr(\widetilde{\mathbf{A}}_n\mathbf{Q})$, i.e., by the sum of the q degrees of freedom from the parametric part of the problem (the number of covariates) and the equivalent degrees of freedom from the non-parametric part of the model, $tr(\widetilde{\mathbf{A}}_n\mathbf{Q})$. This can be used in the estimation of σ and for GCV, as highlighted above. Finally, the predicted value of a new observation at $\mathbf{x}_{n+1}$ with covariates $\mathbf{w}_{n+1}$ is given by $\hat{z}_{n+1} = \mathbf{w}_{n+1}'\hat{\boldsymbol{\beta}} + \hat{f}(\mathbf{u}_{n+1}) = \mathbf{w}_{n+1}'\hat{\boldsymbol{\beta}} + \hat{\mathbf{f}}'\boldsymbol{\psi}(\mathbf{u}_{n+1})$. The mean and variance of the new observation can be obtained from the equations above and an approximate prediction intervals may be derived, likewise.

E Computational algorithm for constructing the flattening map

We approximate the conformal parameters in (7)-(8) in the space $H^1_{\mathcal{T}}(\Sigma)$. The harmonic functions u and v are approximated with functions that are globally continuous and linear over each triangle of $\Sigma_{\mathcal{T}}$. Below, we outline the finite element procedure for the flattening map. Note that one has to be careful in choosing the three-dimensional mesh $\Sigma_{\mathcal{T}}$, because degenerate triangles can be generated by flattening a triangle with all the vertices on the boundary.

1. An approximation of u is found by minimizing $E_D(u)$ in (13) over $H^1_{\mathcal{T}}(\Sigma)$. The energy functional is invariant with respect to conformal changes of the domain metric [19]. This fact yields a convenient cotangent formula for the stiffness matrix D. The entries of D are created by gathering terms that share an edge. That is, if $\mathbf{x}_j$ and $\mathbf{x}_l$ are connected by an edge of the triangular mesh $\Sigma_{\mathcal{T}}$, then $D_{jl} = -\frac{1}{2}(\cot\alpha_j + \cot\beta_j)$ where α_j and β_j are the angles opposite the edge formed by $\mathbf{x}_l$ and $\mathbf{x}_j$. If $\mathbf{x}_j$ and $\mathbf{x}_l$ are not connected by an edge, then $D_{jl} = 0$. The diagonal entries of D are $D_{jj} = -\sum_{l\neq j} D_{jl}$. For the boundary conditions stated in (7), each interior vertex $\mathbf{x}_j \in \Sigma_{\mathcal{T}}$ must satisfy
$$\sum_{\mathbf{x}_l\in\Sigma_{\mathcal{T}}} D_{jl}u_l = -\sum_{\mathbf{x}_l\in b_1} D_{jl}. \tag{24}$$

Solving the system above approximates the conformal parameter u. This linear map conformally maps $\Sigma_{\mathcal{T}}$ to an annulus where b_0 and b_1 are the inner and outer boundaries, respectively. See Figure 4 (right).

2. Cut $\Sigma_{\mathcal{T}}$ along the gradient of u. The maximum principle implies that there always exists a vertex adjacent to the current vertex with a larger value. We use this fact to find the cut C on the surface. Start by picking a vertex on b_0 to be the starting point, call it ζ_0. Search the adjacent vertices and move to the vertex with a larger value of u. Continue to search the vertices adjacent to current vertex; always moving to the vertex with a larger value of u. Once you reach a vertex in b_1 then you have completed the cut.

3. Create the oriented boundary B. Let B start on the vertex ζ_0 from the previous step. Let B run from ζ_0 around b_0 back to ζ_0. Then up the cut C and around b_1 and back down C in the opposite direction back to ζ_0 creating a closed curve. Keep in mind that B must run around b_0 and b_1 in a way that keeps the orientation of the surface. See Figure 4 (center). A programming note: the vertices along C will need to be repeated twice since they will end up on opposite sides of the rectangle.

4. Generate the boundary values for v. Recall, the boundary values for v are found by integrating along B $v(\zeta) = \int_{\zeta_0}^{\zeta} \frac{\partial u}{\partial \nu} ds$ where ds is the arc-length element along B. Since u is harmonic, the divergence theorem yields $\oint_B \frac{\partial u}{\partial \nu} ds = 0$, where $\oint_B$ is the line intergral over the closed boundary B. The cut C is constructed along the gradient of u thus $\frac{\partial u}{\partial \nu} = 0$ along C. Hence v is constant along C. Note that the height of the cylinder must be scaled properly. The height of the cylinder becomes the width of the rectangle which is forced to have length equal to one. Hence the height of the rectangle will be the circumference of the cylinder divided by the height of the cylinder. If the proportions of the rectangle are not scaled properly, then the coordinates (u, v) will not be conformal.

5. Set up and solve the system for v as in Step 1., adjusting the righthand side of (24) to take into account the boundary values for v in (8).

MOX Technical Reports, last issues

Dipartimento di Matematica "F. Brioschi",
Politecnico di Milano, Via Bonardi 9 - 20133 Milano (Italy)

54/2012 Ettinger, B., Perotto, S.; Sangalli, L.M.
Spatial regression models over two-dimensional manifolds

53/2012 Fumagalli, A.; Scotti, A.
An efficient XFEM approximation of Darcy flows in fractured porous media

52/2012 Perotto, S.
Hierarchical model (Hi-Mod) reduction in non-rectilinear domains

51/2012 Beck, J.; Nobile, F.; Tamellini, L.; Tempone, R.
A quasi-optimal sparse grids procedure for groundwater flows

50/2012 Carcano, S.; Bonaventura, L.; Neri, A.; Esposti Ongaro, T.
A second order accurate numerical model for multiphase underexpanded volcanic jets

49/2012 Migliorati, G.;Nobile, F.;von Schwerin, E.;Tempone, R.
Approximation of Quantities of Interest in stochastic PDEs by the random discrete L2 projection on polynomial spaces

48/2012 Ghiglietti, A.; Paganoni, A.M.
Statistical properties of two-color randomly reinforced urn design targeting fixed allocations

47/2012 Astorino, M.; Chouly, F.; Quarteroni, A.
Multiscale coupling of finite element and lattice Boltzmann methods for time dependent problems

46/2012 Dassi, F.; Perotto, S.; Formaggia, L.; Ruffo, P.
Efficient geometric reconstruction of complex geological structures

45/2012 Negri, F.; Rozza, G.; Manzoni, A.; Quarteroni, A.
Reduced basis method for parametrized elliptic optimal control problems